Power Electronic Systems
Laboratory

IEEE Transactions on Industrial Electronics, Vol. 61, No. 8, pp. 4326-4336, August 2014

Analysis and Design of a 300-W 500 000-r/min Slotless Self-Bearing Permanent-Magnet Motor

T. Baumgartner,
R. Burkar,
J. W. Kolar

Eidgenössische Technische Hochschule Zürich
Swiss Federal Institute of Technology Zurich

Analysis and Design of a 300-W 500 000-r/min Slotless Self-Bearing Permanent-Magnet Motor

Thomas Baumgartner, *Student Member, IEEE*, Ralph M. Burkart, *Student Member, IEEE*, and Johann W. Kolar, *Fellow, IEEE*

***Abstract*—Active magnetic bearings enable contactless operation and can therefore be used for supporting rotors spinning at high speeds. However, the rotational speed in conventional reluctance-force-based magnetic bearing topologies is limited, which is mainly due to high rotor losses and limited force control bandwidths. In this paper, a prototype of a self-bearing motor is presented, which overcomes several limitations of state-of-the-art high-speed magnetically levitated electric drive systems. Due to the employed magnetic bearing, the motor can be operated in high-purity or vacuum environments. An analytical mechanical and electrical bearing model is introduced and verified by measurements. Furthermore, a bearing inverter system is designed, and its controller performance is shown. Measurements of spinning levitated rotors up to speeds of 505 000 r/min verify the functionality of the overall system. To the authors' knowledge, this is the highest speed achieved by magnetically levitated electrical drive systems so far.**

***Index Terms*—Active magnetic bearing (AMB), bearing inverter system, bearingless drive, deceleration test, Lorentz actuator, permanent-magnet synchronous motor (PMSM), rotor bending resonance measurement, slotless magnetic bearing, vacuum.**

NOMENCLATURE

B, $\boldsymbol{B}$, $\hat{B}$	Magnetic flux density, vector, amplitude.
B_{rem}	Remanent flux density.
e	Euler's number.
e	Control error.
$\boldsymbol{F}$	Force vector.
$\boldsymbol{H}$	Magnetic field vector.
i, $\underline{i}$, $\hat{i}$	Winding current, space vector, amplitude.
j	Imaginary unit.
$\boldsymbol{J}$, $\underline{J}$, $\hat{J}$	Current density vector, space vector, amplitude.
k	Inductance coupling factor.
K_{P}	Proportional controller gain.
L	Axial winding length.
L_{S}	Transformed stator phase inductance.
m	Phase number.
N	Number of winding turns.
p_{pm}	Rotor pole-pair number.
p_{w}	Winding pole-pair number.
(r, θ, z)	Cylindrical coordinates.
R_1	Permanent-magnet radius.
R_2	Rotor outer radius.
R_3	Bearing winding inner radius.
R_4	Bearing winding outer radius.
R_6	Stator-core inner radius.
R_{S}	Stator phase resistance.
s	Laplace variable.
$\boldsymbol{T}$	Torque vector.
T_{del}	Delay time.
T_{I}	Integral controller time constant.
u, $\underline{u}$	Voltage, space vector.
(x, y, z)	Cartesian coordinates.
x_{B}, y_{B}	Rotor displacements.
γ	Angular orientation of the remanent flux density.
ε	Phase of the winding current space vector.
μ	Permeability.
χ_{pm}	Radial bearing constant.
ψ_{pm}, $\underline{\psi}_{\mathrm{pm}}$	Flux linkage, space vector.
Ω	Angular frequency of the rotor.

Subscripts

d	Direct-axis component.
L	Lorentz force.
ph	Phase.
q	Quadrature-axis component.
R	Reluctance force.
ref	Reference.
S	Stator.

Manuscript received January 30, 2013; revised July 15, 2013 and August 22, 2013; accepted September 4, 2013. Date of publication October 1, 2013; date of current version February 7, 2014.

The authors are with the Power Electronic Systems Laboratory, Swiss Federal Institute of Technology (ETH) Zurich, CH-8092 Zurich, Switzerland (e-mail: baumgartner@lem.ee.ethz.ch; burkart@lem.ee.ethz.ch; kolar@lem.ee.ethz.ch).

Color versions of one or more of the figures in this paper are available online at http://ieeexplore.ieee.org.

Digital Object Identifier 10.1109/TIE.2013.2284159

I. INTRODUCTION

ULTRAHIGH-SPEED electrical drive systems are developed for new emerging applications, such as turbo compressor systems, ultracentrifuges, rotating mirrors in optical applications, and milling spindles. Several studies on the design and speed limitations of ultrahigh-speed electrical drive systems have been recently published [1]–[3]. Most systems built today rely on ball bearings for rotor support. In many applications, the ball bearings are limiting the lifetime of a system [1]. Several applications, such as optical scanning systems or reaction wheels for attitude control of satellites in orbit, require a lifetime of several thousand hours and the operation in vacuum. These requirements exclude bearing technologies such as ball bearings or gas bearings. The use of active magnetic

bearings (AMBs) enables contactless operation and the operation in vacuum. Furthermore, rotor dynamics can be actively controlled, allowing canceling or damping of instabilities.

Most AMB systems built today rely on reluctance force, which is generated by guiding a magnetic flux over the air gap between the rotor and the stator. This flux is actively controlled by controlling the bearing winding currents. In the present paper, this bearing topology will be referred to as reluctance-force-based AMB. In contrast, Lorentz-force-based AMB rely on an external magnetic flux density (typically generated by a set of permanent magnets on the rotor) and electric current densities in bearing windings. The windings are placed in the magnetic air gap of the external flux density. Thus, the bearing force generation is mainly based on Lorentz force in the bearing windings.

There are several AMB designs proposed in literature for speeds beyond 100 000 r/min. However, there are only few publications with experimental results. Reluctance-force-based homopolar bearings are presented in [4] and [5]. In [4], a magnetically levitated milling spindle that achieved a speed of 150 kr/min is presented. In [5], a 2-kW machine was operated up to a speed of 120 kr/min. However, all reluctance-force-based AMB systems suffer from iron losses on the rotor [6]. Even homopolar bearings, which are optimized for low rotor losses, suffer from speed-dependent slot-harmonic induced losses [4], [5]. Due to the poor thermal coupling of the levitated rotor to the rest of the drive system, these losses are crucial. In many AMB applications, the maximum rotational speed is limited by the rotor losses [6]. Furthermore, eddy currents in the magnetic circuit limit the achievable actuator bandwidth [6].

One possibility to overcome the problem of high rotor losses is to rely on Lorentz forces for bearing force generation. Although the achievable maximum bearing forces are small compared with reluctance-force-based bearings, the concept of Lorentz-force-based bearings enables high-speed rotation when properly designed [7]. A slotless and, thus, Lorentz-force-based high-speed self-bearing motor is presented in [8]. In contrast to the design proposed in this paper, a short (slice) rotor was chosen in [8]. Three degrees of freedom (DOFs) of the rotor are actively controlled by a combined motor-bearing winding, whereas three DOFs are passively stabilized by reluctance forces [8]. The achieved speed of 115 kr/min is limited by the mechanical construction of the rotor [8]. One possibility to reach higher speeds is by implementing a scaled-down version of the slice motor. However, the downscaling is limited by the passive stabilization of three DOFs. More applications on slotless self-bearing motors designed for lower speeds are presented in [9] and [10] for positioning applications. Low-speed self-bearing slice motors for mixing applications are presented in [11] and [12]. A single-DOF actively positioned self-bearing motor is presented in [13]. In [14], a nonsalient permanent-magnet axial-gap self-bearing motor is proposed, combining the axial bearing and the motor.

In 1946, a rotational speed of 23 million r/min was achieved by a small magnetically levitated steel ball [15]. The highest rotational speed of any macroscopic object was achieved in [16] by spinning graphene flakes at rotational speeds of up to 60 million r/min. In this paper, the physical experiments presented in [15]–[17] will not be considered electric drive systems because they have no possibility of driving an application.

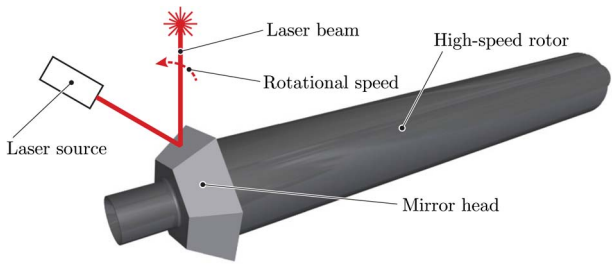

Fig. 1. High-speed rotor of one possible application of the presented prototype in laser scanning systems. The six-faced mirror head deviates a laser beam periodically over a scanning angle of 60° with a repetition frequency of 48 kHz.

A. Contributions and Outline of the Paper

In this paper, a self-bearing machine designed for rotational speeds of up to 500 kr/min and a rated machine power of 300 W is presented, and measurement results are shown. In contrast to state-of-the-art designs, the ironless construction of the rotor and the slotless design of the stator enable ultrahigh-speed rotation and very high bearing actuator bandwidths. Thus, the presented prototype overcomes several limitations of previously presented AMB systems. All six DOFs of the rotor are actively controlled by Lorentz forces generated by air-gap windings.

The machine is designed for driving optical components, such as mirrors in laser scanning applications. In this application, a lifetime of several thousand hours at speeds of 200–500 kr/min is required. Furthermore, the rotor has to be operated in a hermetically sealed containment to prevent defilement of the optical components. Due to the long lifetime requirement, only contactless bearing technologies come into consideration. Static gas bearings are not considered as they require an external pressure supply. Thus, the only bearing technologies that can be applied in this application are the dynamic gas bearing and the magnetic bearing. Typically, gas bearings can be realized very compactly with high load capacity and stiffness. However, poor dynamic stability has been limiting their use at high rotational speeds [18]. In this paper, AMBs were selected since they fulfill the application requirements and allow actively controlling the dynamics of the rotor. The drawback, when compared with dynamic gas bearings, is the higher complexity of the drive system.

The rotor of one possible application of the presented prototype is depicted in Fig. 1. The six-faced mirror head is used for the periodic deviation of a laser beam. With this setup, a laser beam of a maximum diameter of 3 mm can be periodically deviated over a scanning angle of 60°. A rotor dynamical analysis shows that a rotor of these dimensions can be operated up to 480 kr/min. Thus, a very high repetition frequency of 48 kHz can be achieved. The ultrahigh rotational speed is chosen in order to increase the scanning speed of the laser scanner.

A preliminary version of this paper was presented in [19] at the 38th Annual Conference of the IEEE Industrial Electronics Society (IECON 2012). The maximum speed achieved in [19]

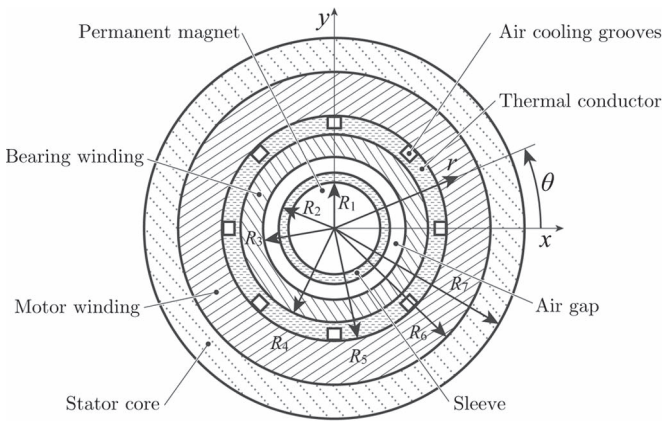

Fig. 2. Cross section of the machine and symbol definitions: cylindrical permanent-magnet rotor inside a slotless stator core.

TABLE I
PROPERTIES OF THE IMPLEMENTED MACHINE PROTOTYPE

Symbol	Quantity	Value
$n_{\max}$	Maximum rotational speed	500 000 rpm
P_{rated}	Rated motor power	300 W
$\psi_{\text{pm,motor}}$	Motor flux linkage	$0.40 \cdot 10^{-3}$ Vs
R_1	Permanent-magnet radius	3 mm
R_2	Rotor outer radius	3.65 mm
R_6	Stator-core inner radius	12 mm
L_{rotor}	Total rotor length	55 mm
m_{rotor}	Rotor mass	12.3 g
B_{rem}	Remanent flux density	1.07 T

was limited by the rotor construction. The results presented in this paper are based on an improved rotor construction and control strategy. This allows operating the prototype up to its rated speed.

II. Machine Design and Operating Limitations

The concept of the implemented prototype is based on a magnetically levitated permanent-magnet synchronous motor. The integrated machine and bearing concept was proposed in [7], and a working prototype was presented in [19].

The cross section of the machine is shown in Fig. 2. The dimensions and properties of the implemented prototype can be found in Table I. A CAD sectional view of the machine is depicted in Fig. 3, and a picture of the implemented test bench is shown in Fig. 4.

A rotor containing an axially magnetized permanent magnet and two diametrically magnetized permanent magnets is inserted into a slotless amorphous-iron stator core. The magnetic air gap between the rotor and the stator core is used to place a motor winding and three bearing windings. The radial bearing windings are manufactured as skewed air-gap windings, as defined in [20]. A grooved tube of thermally conductive but electrically isolating polymer is inserted between the bearing and the motor winding, allowing cooling the windings with pressurized air during the operation. The rotor is encapsulated by a sealed PEEK tube to operate the rotor in vacuum (not shown in Fig. 2). The vacuum sealing and the ISO-KF vacuum

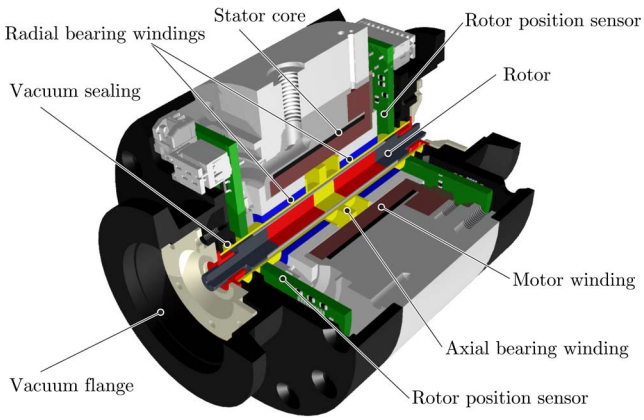

Fig. 3. Sectional view of the high-speed self-bearing machine prototype.

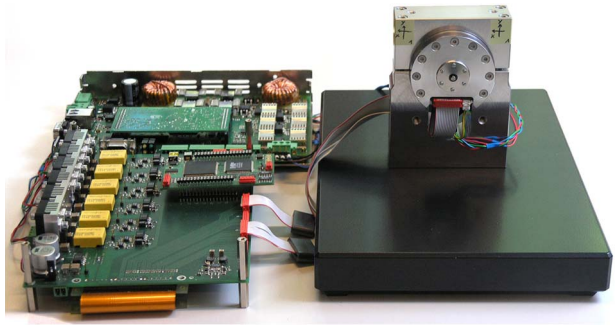

Fig. 4. Implemented self-bearing machine test bench with bearing and motor inverters.

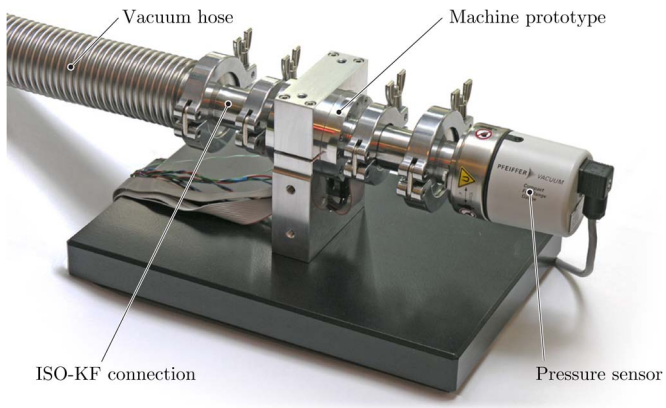

Fig. 5. Picture of the implemented self-bearing machine test bench with vacuum connections and sensors.

flanges are shown in Fig. 3. A picture of the machine prototype with vacuum connections is shown in Fig. 5.

For the control of the magnetic bearing, printed-circuit-board (PCB)-based rotor position sensors are placed on both sides of the motor. The radial rotor position is measured based on eddy-current sensors, whereas the axial and angular positions are obtained by Hall-effect-based stray-field measurements. A cascaded control scheme, as proposed in [19], is employed for the AMB control. The rotor position is controlled in an outer control loop, whereas the winding currents are tracked in an inner field-oriented control loop, as described in Section IV-B. The design of the rotor position controller is beyond the scope

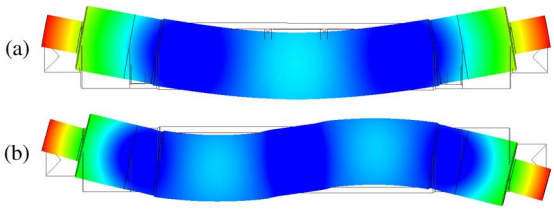

Fig. 6. (a) First bending mode of the rotor with a resonance frequency of 11.9 kHz (standstill). (b) Second bending mode with a resonance frequency of 27.7 kHz (standstill).

of this paper. An analysis of the implemented controller is presented in [21].

The proposed machine topology features a set of advantages and disadvantages when compared with state-of-the-art reluctance-force-based AMB designs. The main advantage is the low high-frequency power loss. In particular, low rotor losses, resulting from the slotless construction of the stator and the ironless construction of the rotor, enable ultrahigh-speed rotation. Due to the slotless winding design, the winding fields are small when compared with slotted designs. This yields negligible rotor eddy-current losses. In contrast to reluctance-force-based AMB, the proposed bearing actuators are based on Lorentz force, i.e., the achievable actuator bandwidth is not limited by eddy currents in the rotor iron. Furthermore, small winding inductances follow from the slotless design. The concept of using separate bearing and motor windings yields low induced voltages in the bearing windings. It is shown in Section IV that these features enable to control the bearing currents and, thus, also the bearing forces up to high bandwidths with low reactive power consumption. The inverters can be implemented using low-voltage power electronics, enabling ultrafast switching frequencies. The drawback of the proposed Lorentz-force-based bearing actuators is the comparably low load capacity of the magnetic bearing.

The maximum speed of the machine is limited by the mechanical design and the dynamics of the rotor. In particular, the material stresses and the frequency of the rotor bending modes limit the rotational speed. When a rotor for a certain speed is designed, the rotor diameter is limited by the maximum tolerable stresses at the maximum speed. Similarly, the rotor length is limited by the minimum tolerable frequency of the first bending mode. Rotor unbalances excite the rotor system at the frequency of rotation [6]. In the implemented prototype, the unbalance excitation cannot be compensated by the magnetic bearing, and the rotor cannot be accelerated fast enough through the bending resonance. Therefore, the maximum rotational frequency must not exceed the frequency of the first bending mode. Fig. 6 shows the result of a finite-element modal analysis calculated using the commercial software ANSYS. The result features a frequency gap between the first bending mode frequency of 11.9 kHz and the frequency of the unbalance excitation of 8.33 kHz at the rated rotational speed. The modal analysis is verified by measurements in Section V-C.

The limitation of the machine power is given by the thermal design. The limitation is a result of the power loss in the motor winding, the temperature rating of the used materials, the thermal resistance to the stator housing, and the cooling capacity of the stator housing. The implemented prototype machine was designed for a machine power of 300 W. The maximum winding temperature for this load situation of 120 °C is calculated by a finite-element method (FEM) simulation. The electromagnetic and thermal design of the motor winding is beyond the scope of this paper. The interested reader is referred to [1] for a detailed analysis. The motor flux linkage of the machine is given in Table I. It is calculated using the analytical solution presented in [22].

III. Radial Bearing Design

In the following analysis, vectors, such as 3-D force vectors, will be denoted by bold letters (e.g., $\boldsymbol{F}$), whereas stator-fixed space vectors, which are transformed by the amplitude-invariant Clarke transformation, will be denoted by underlined letters (e.g., $\underline{J}_{\mathrm{S}}$).

The electromagnetic force and torque on a rotor of an electric machine can be calculated by integrating the local stator reaction force density $d\boldsymbol{F}_{\mathrm{S}}$ over the volume V of the stator, i.e.,

$$\boldsymbol{F} = -\iiint_V d\boldsymbol{F}_{\mathrm{S}} = -\iiint_V d\boldsymbol{F}_{\mathrm{L,S}} + d\boldsymbol{F}_{\mathrm{R,S}}). \tag{1}$$

The minus sign follows from the third of Newton's laws of motion. The force density $d\boldsymbol{F}_{\mathrm{S}}$ can be further split up into a Lorentz force component

$$d\boldsymbol{F}_{\mathrm{L,S}} = \boldsymbol{J} \times \boldsymbol{B} \cdot dV \tag{2}$$

and a reluctance force component

$$d\boldsymbol{F}_{\mathrm{R,S}} = \frac{1}{2}\boldsymbol{H}^2 \cdot \boldsymbol{\nabla}\mu \cdot dV \tag{3}$$

where $\boldsymbol{J}$ is the current density, $\boldsymbol{B}$ is the magnetic flux density, $\boldsymbol{H}$ is the magnetic field, and $\boldsymbol{\nabla}\mu$ is the gradient of the local permeability. In regions with constant permeability μ, the reluctance force density $d\boldsymbol{F}_{\mathrm{R,S}} = 0$ vanishes. Therefore, in many slotless machine designs, the only area where reluctance forces occur is the inner surface of the stator core.

In [20], an analysis of Lorentz forces generated in slotless skewed bearing and motor windings is presented. However, in [20], the reluctance force resulting from high-permeability stator cores is not considered.

A. Permanent-Magnet Flux Density Distribution

The permanent-magnet flux density in the air gap of a slotless machine for a radially centered rotor can be described in cylindrical coordinates (r, θ, z) by Fourier series for both the radial and azimuthal field components [23]. For the scope of this paper, the harmonic components of the permanent-magnet field are omitted. Thus, a purely sinusoidal field distribution

$$B_r = \hat{B}_r(r) \cdot \cos\left(p_{\mathrm{pm}}(\theta - \gamma)\right) \tag{4}$$

$$B_\theta = \hat{B}_\theta(r) \cdot \sin\left(p_{\mathrm{pm}}(\theta - \gamma)\right) \tag{5}$$

is assumed, where p_{pm} is the rotor pole-pair number, and γ is the angular orientation of the remanent flux density of the permanent magnet in the xy plane. In the following subsections,

the configuration $p_{\mathrm{pm}} = 1$ is analyzed in more details. This field distribution is achieved with the use of a cylindrical diametrically magnetized permanent magnet [1]. The field in axial direction is assumed to be $B_z = 0$.

B. Analytic Lorentz Force Calculation

Here, analytical results are presented for the Lorentz force vector generated by skewed bearing windings. The analysis is based on the integration of the Lorentz force density over the stator volume. Thereby, the reluctance force caused by the stator core and the armature reaction is neglected. Although the presented results are only correct for ironless designs, they still illustrate the generation of bearing force what will be the basis of the current and position controllers used to operate the motor. Results, including reluctance force, which are presented in Section III-C, show that the influence of reluctance force can be neglected for sufficiently large ratios of R_6/R_4.

The winding parameterization and detailed calculations for this type of winding are given in [22]. A winding is defined by the number of pole pairs p_{w} and the number of phases m. For the radial bearing winding, the configuration $p_{\mathrm{w}} = 2$, $m = 3$, and $p_{\mathrm{pm}} = 1$ is chosen. According to [22], the amplitude-invariant current density space vector

$$\underline{J}_{\mathrm{S}} = \hat{J}_{\mathrm{S}} \mathrm{e}^{\mathrm{j}\varepsilon} = \frac{3\pi N \cdot \hat{i}_{\mathrm{S}} \mathrm{e}^{\mathrm{j}\varepsilon}}{\left(\sqrt{4L^2 + \pi^2 R_4^2} - \sqrt{4L^2 + \pi^2 R_3^2}\right)} \tag{6}$$

can be defined, with N, L, and j being the number of winding turns per phase and pole, the axial winding length, and the imaginary unit, respectively. $\hat{i}_{\mathrm{S}}$ denotes the amplitude of the winding current space vector, and ε denotes its phase. In [20], it was shown that, for a radially centered rotor, the integration of the Lorentz force density over the phase belt of one phase and a subsequent summation over m phases yields a vanishing torque $\boldsymbol{T}_{\mathrm{L}} = \mathbf{0}$ and the force vector

$$\boldsymbol{F}_{\mathrm{L}} = \frac{2m \sin\left(\frac{\pi}{m}\right) L^2}{\pi} \int_{R_3}^{R_4} \frac{\left(\hat{B}_r + \hat{B}_\theta\right) r \, dr}{\sqrt{4L^2 + \pi^2 r^2}} \begin{bmatrix} \hat{J}_{\mathrm{S}} \cos(\varepsilon - \gamma) \\ \hat{J}_{\mathrm{S}} \sin(\varepsilon - \gamma) \\ 0 \end{bmatrix} \tag{7}$$

given in Cartesian coordinates (x, y, z). The integration over r is solved using the field solution for $\hat{B}_r$ and $\hat{B}_\theta$ presented in [1]. Finally, the bearing force can be expressed by

$$\boldsymbol{F}_{\mathrm{L}} = \frac{3}{2} \chi_{\mathrm{pm,L}} \begin{bmatrix} \hat{i}_{\mathrm{S}} \cos(\varepsilon - \gamma) \\ \hat{i}_{\mathrm{S}} \sin(\varepsilon - \gamma) \\ 0 \end{bmatrix} \tag{8}$$

with the Lorentz bearing constant

$$\chi_{\mathrm{pm,L}} = \frac{3\sqrt{3} N K_{\mathrm{B2}} R_6^2}{\sqrt{4L^2 + \pi^2 R_4^2} - \sqrt{4L^2 + \pi^2 R_3^2}} \cdot K_1 \tag{9}$$

and K_1 defined as

$$K_1 = \log\left(\frac{2L + \sqrt{4L^2 + \pi^2 R_3^2}}{2L + \sqrt{4L^2 + \pi^2 R_4^2}} \cdot \frac{2L - \sqrt{4L^2 + \pi^2 R_4^2}}{2L - \sqrt{4L^2 + \pi^2 R_3^2}}\right). \tag{10}$$

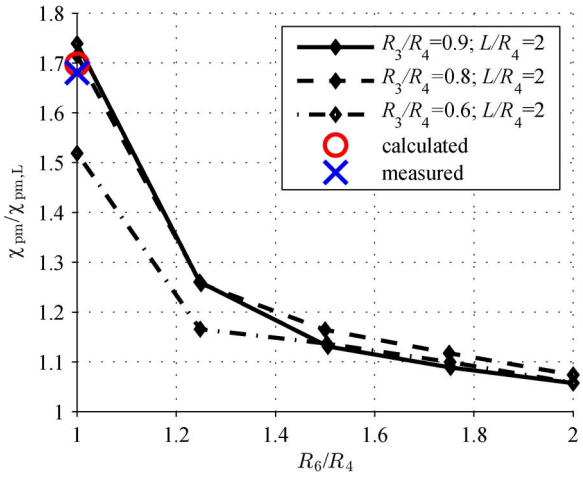

Fig. 7. Ratio of the bearing constant χ_{pm} including reluctance force to the bearing constant $\chi_{\mathrm{pm,L}}$ calculated by (9) solely based on Lorentz force. The cross marks the 3-D measurement of total bearing force measured by a piezoelectric multicomponent dynamometer for the geometry $R_3/R_4 = 0.8$, $L/R_4 = 2.75$, and $R_6/R_4 = 1$. The circle marks the FEM-calculated value for the same geometry.

The calculation of K_{B2} is presented in [1]. To facilitate its calculation, it can be assumed that the relative permeability of the permanent magnet and the stator core are $\mu_{\mathrm{r,pm}} \approx 1$ and $\mu_{\mathrm{r,Fe}} \to \infty$ [7], respectively, which yields

$$K_{\mathrm{B2}} = \frac{B_{\mathrm{rem}} R_1^2}{2R_6^2}. \tag{11}$$

C. Three-Dimensional FEM Calculations of the Bearing Forces

The bearing force calculation presented in the previous subsection is based on Lorentz force solely. With the presence of an iron stator core, the analysis must also include reluctance forces. Therefore, a magnetostatic FEM calculation is used to determine the magnetic field generated by the winding.

The 3-D winding field distribution is calculated using the commercial FEM software COMSOL. Thereby, the cylindrical stator core is modeled as a linear material with a relative permeability $\mu_{\mathrm{r,Fe}} = 1000$. The total flux density in the air gap of the bearing is given by the superposition of the winding flux density and the flux density caused by the permanent magnet, for which again the analytical 2-D model in [1] is used. As proposed in [22], the bearing force is then obtained by numerical integration of the Maxwell stress tensor evaluated for the total flux density on the cylindrical surface with radius R_2.

The FEM calculation yields an increased bearing force with the presence of an iron stator core. The increase in the total force compared with the analytically calculated Lorentz force is shown in Fig. 7 for different bearing geometries. In the presented prototype, the ratio is $R_6/R_4 = 2$. Thus, it is expected that the total bearing constant χ_{pm} is approximately 7% greater than $\chi_{\mathrm{pm,L}}$ calculated by (9). Note that this is not the same geometry as the measured geometry shown in Fig. 7.

D. Electrical Bearing Model

In order to control the bearing force $\boldsymbol{F}$, the bearing currents have to be controlled. For the design of the bearing inverter and the corresponding current controller, the electric model of the bearing has to be analyzed in more detail. In operation of the magnetic bearing, small radial rotor displacements x_B and y_B may occur. The permanent-magnet flux linkage space vector in the magnetic bearing winding is given by

$$\underline{\psi}_\mathrm{pm} = \chi_\mathrm{pm}(x_\mathrm{B} + \mathrm{j}y_\mathrm{B})\mathrm{e}^{\mathrm{j}\gamma} \tag{12}$$

for small rotor displacements. The bearing has a symmetrical magnetic construction; the small difference in permeability in the magnet magnetization axis and orthogonal thereto is negligible. Therefore, the bearing winding voltage space vector is defined as

$$\underline{u}_\mathrm{S} = R_\mathrm{S}\underline{i}_\mathrm{S} + \frac{\partial}{\partial t}\left(L_\mathrm{S}\underline{i}_\mathrm{S} + \underline{\psi}_\mathrm{pm}\right) \tag{13}$$

where $\underline{i}_\mathrm{S}$ is the bearing current space vector, R_S is the stator phase resistance, and L_S is the equivalent decoupled stator phase inductance.

However, for control purposes, the stator-fixed quantities are preferably written in a rotor-fixed coordinate system. This is achieved by expressing $\underline{u}_\mathrm{S} = (u_d + \mathrm{j}u_q)\mathrm{e}^{\mathrm{j}\gamma}$ and $\underline{i}_\mathrm{S} = (i_d + \mathrm{j}i_q)\mathrm{e}^{\mathrm{j}\gamma}$ by rotor-fixed real-valued dq quantities. Thus, (13) can be written as

$$u_d = R_\mathrm{S}i_d + L_\mathrm{S}\left(\frac{\partial i_d}{\partial t} - \Omega i_q\right) + \chi_\mathrm{pm}\left(\frac{\partial x_\mathrm{B}}{\partial t} - \Omega y_\mathrm{B}\right) \tag{14}$$

$$u_q = R_\mathrm{S}i_q + L_\mathrm{S}\left(\frac{\partial i_q}{\partial t} + \Omega i_d\right) + \chi_\mathrm{pm}\left(\frac{\partial y_\mathrm{B}}{\partial t} + \Omega x_\mathrm{B}\right) \tag{15}$$

where $\Omega = (\partial\gamma)/(\partial t)$ is the angular frequency of the rotor. The instantaneous bearing power is given by

$$\frac{3}{2}\Re\left(\underline{u}_\mathrm{S}\underline{i}_\mathrm{S}^*\right) = \frac{3}{2}\Re\left(R_\mathrm{S}|\underline{i}_\mathrm{S}|^2 + L_\mathrm{S}\frac{\partial \underline{i}_\mathrm{S}}{\partial t}\underline{i}_\mathrm{S}^*\right) + \boldsymbol{F}\cdot\begin{bmatrix}\frac{\partial x_\mathrm{B}}{\partial t}\\ \frac{\partial y_\mathrm{B}}{\partial t}\\ 0\end{bmatrix} + \boldsymbol{T}\cdot\begin{bmatrix}0\\0\\\Omega\end{bmatrix} \tag{16}$$

where $\Re(\ldots)$ denotes the real part of a space vector, and $\underline{i}_\mathrm{S}^*$ denotes the complex conjugate of $\underline{i}_\mathrm{S}$. The resulting bearing force

$$\boldsymbol{F} = \frac{3}{2}\chi_\mathrm{pm}\begin{bmatrix}i_d\\ i_q\\ 0\end{bmatrix} \tag{17}$$

can be derived from solving (16). Furthermore, it can be seen that an undesirable drive torque

$$\boldsymbol{T} = \frac{3}{2}\chi_\mathrm{pm}\begin{bmatrix}0\\0\\x_\mathrm{B}i_q - y_\mathrm{B}i_d\end{bmatrix} \tag{18}$$

occurs when the rotor is deviated radially. For applications where a very accurate control of the angular frequency Ω is required, this torque can be compensated by the motor winding.

IV. Power Electronics

A. Specifications

The electrical bearing model (14), (15), (17) implies the need for three-phase sinusoidal bearing currents to control the rotor position. Hence, a suitable inverter system is required, which meets the following specifications.

- Extensive simulations have been performed to determine the range of applicable bearing forces $\boldsymbol{F}$, which are required to stabilize and adequately control the rotor up to the target rotational speed of 500 kr/min ($\Omega = 2\pi \cdot 8.33$ kHz). Using (9), (10), and (17), the number of winding turns N and the geometry of the bearing winding have been chosen to obtain currents in the low ampere-range. Finally, using (14) and (15) yields that a peak output voltage $|\underline{u}_\mathrm{S}|_\mathrm{max}$ of 6 V is sufficient for the entire range of operation. The chosen current and voltage ratings allow for a greatly simplified inverter implementation, as further described in Section IV-B.
- Ripple currents deviating from the desired reference values do not contribute to a useful net bearing force but increase the ohmic losses in the windings. Therefore, such currents must be minimized in order not to compromise the maximum applicable forces.
- In motor drive applications, errors in the relative current orientation $\varepsilon - \gamma$ lead to (normally) insignificant torque *amplitude* errors. In contrast, for the bearing application at hand, relative current orientation errors result in wrong bearing force *directions* [cf. (8)]. Simulations have shown that such direction errors can severely compromise the performance of the position controller and cause instability. Consequently, as the current control actions are performed in dq coordinates, it is crucial that the employed coordinate transformations between dq and stator-fixed coordinates are based on precise current and angular rotor position measurements. Furthermore, these transformations must be updated at high sampling rates to keep the orientation errors small.
- A controller architecture with the rotor position controller in the outer and subordinate bearing current controllers in the inner loop is proposed [19]. As a consequence of this cascaded approach, a minimum current controller bandwidth $f_\mathrm{bw} = 12$ kHz was identified in simulations to achieve satisfactory control performance. This bandwidth requirement is equivalent to a loop delay of several microseconds in case of a standard proportional–integral (PI) current control scheme.

B. Implementation

1) Inverter Topology: The inverter system was implemented using a three-phase two-level voltage source inverter (2LVSI) topology, as depicted in Fig. 8. The simple topology and, in

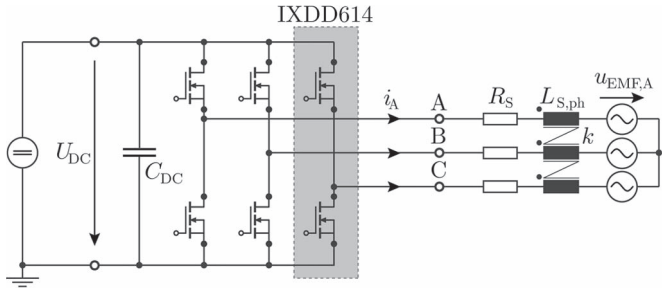

Fig. 8. 2LVSI topology for one radial bearing and equivalent circuit of the bearing winding. The employed gate driver ICs consist of a p- and n-channel MOSFET ($R_{\mathrm{ds,on}} = 0.4\ \Omega$). $\underline{u}_{\mathrm{EMF}} = (\partial/(\partial t))\underline{\psi}_{\mathrm{pm}}$ is the back EMF voltage, and $L_{\mathrm{S,ph}}$ are the mutually coupled stator phase inductances ($L_{\mathrm{S}} = L_{\mathrm{S,ph}}(1+k)$).

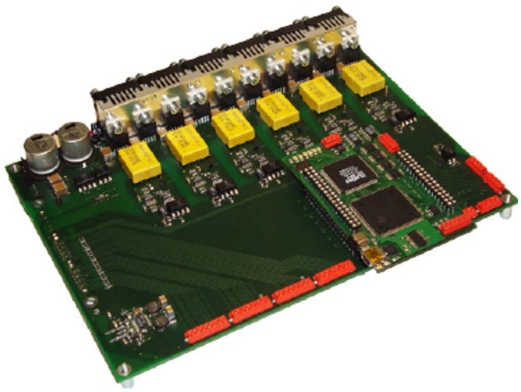

Fig. 9. Implemented bearing inverter system prototype.

contrast to conventional motor drive applications, low current and voltage rating requirements allow using high-speed gate driver integrated circuits (ICs), instead of discrete MOSFETs, for the implementation of the inverter half-bridges. On one hand, such devices can be operated at a very high switching frequency f_{sw}. High switching frequencies enable small bearing current ripples and, thus, low undesired extra losses in the winding. On the other hand, by using gate driver ICs, the system complexity can be highly reduced and a compact design can be achieved. Fig. 9 shows the implemented inverter system. The power electronics consist of two 2LVSIs for the two radial bearings, as well as an additional full-bridge inverter for the axial bearing. All inverter half-bridges are implemented with IXYS IXDD614 gate drivers ($R_{\mathrm{ds,on}} = 0.4\ \Omega$) and share a common dc-link capacitance C_{DC}. The implemented inverter system is capable of impressing 5-A peak bearing currents up to the target rotational speed ($\Omega = 2\pi \cdot 8.33$ kHz) and up to switching frequencies $f_{\mathrm{sw}} = 1$ MHz. The dc-link voltage U_{DC} is adjustable between 10 and 35 V.

2) Measurements: Two currents i_{A} and i_{C} and the rotor position γ are measured to perform the current control in dq coordinates. Due to the very high rotor speeds, small differences between the delay of the current $T_{\mathrm{del},i}$ and the angular rotor position measurements $T_{\mathrm{del},\gamma}$ cause large errors in the measured relative current orientation $\varepsilon - \gamma$ and thus compromise the position control. Therefore, the two measurements must be time synchronized, which is achieved by using a predicted rotor position $\hat{\gamma}$ for the transformation from stator-fixed to dq coordinates, i.e.,

$$\hat{\gamma} = \gamma + \Omega(T_{\mathrm{del},\gamma} - T_{\mathrm{del},i}). \tag{19}$$

The back transformation into stator-fixed coordinates is analogously implemented considering the delay of the control algorithm.

3) Control: A fully field-programmable gate array (FPGA)-based (Cyclone IV) controller is proposed, which offers the advantage of running several current controllers in a simultaneous and time-synchronous manner at high sampling rates. A subharmonic sinusoidal pulsewidth modulation (PWM) scheme is employed. A tradeoff between the number of discrete voltage levels of the associated carrier signal and the achievable switching frequency has been identified due to the high but limited maximum clock rate of the FPGA (300 MHz). The current controllers are implemented as decoupled PI controllers with feedforward terms, i.e.,

$$\underline{u}_{\mathrm{ref}} = \underbrace{\frac{K_{\mathrm{P}}(1+sT_{\mathrm{I}})}{s^2 T_{\mathrm{I}}}\begin{bmatrix} e_d \\ e_q \end{bmatrix}}_{\text{PI controllers}} + \underbrace{L_{\mathrm{S}}\Omega\begin{bmatrix} -i_q \\ i_d \end{bmatrix}}_{\text{decoupling}} + \underbrace{\chi_{\mathrm{pm}}\Omega\begin{bmatrix} -y_{\mathrm{B}} \\ x_{\mathrm{B}} \end{bmatrix}}_{\text{feedforward}}. \tag{20}$$

The main difference to standard synchronous frame PI controllers in motor drive applications, e.g., in [24], is the feedforward terms due to the back electromotive force (EMF) voltage. In the case at hand, not only the rotational speed but also the radial rotor displacements and speeds must be known to correctly compensate the induced voltages $\underline{u}_{\mathrm{EMF}} = (\partial/(\partial t))\underline{\psi}_{\mathrm{pm}}$ [cf. (14) and (15)]. It was observed in simulations that the radial-speed-dependent induced voltages lie in the range of the target voltage quantization of the implemented PWM scheme. For simplicity reasons, these voltages are thus neglected. In contrast, the induced voltages due to radial displacements x_{B}, y_{B} can reach up to 1 V and are, hence, compensated in (20).

With a total adjustable loop delay between 2 and 6 μs (depending on the current filtering), the current controller can achieve a bandwidth of up to $f_{\mathrm{bw}} = 20$ kHz without significant overshoots. Eventually, the high switching frequency in conjunction with the high sampling rate of the back transformation into stator-fixed coordinates reduces the error in the relative current orientation $\varepsilon - \gamma$ to a minimum.

V. Measurements

Here, a set of measurements that are relevant to the machine design and that show the performance of the overall system is presented. In Section V-A, the mechanical bearing model is verified by force measurements. In Section V-B, the controller performance of the bearing inverter system is shown. Section V-C revises the presented modal rotor analysis. The 500-kr/min measurements and no-load power loss measurements are presented in Sections V-D and V-E, respectively. Except for the force measurements in Section V-A, all measurements are performed on the prototype whose mechanical and electrical parameters are given in Tables I and II.

TABLE II
BEARING INVERTER SYSTEM PARAMETERS

Symbol	Quantity	Value
R_S	Stator phase resistance	$1.1\,\Omega$
L_S	Transformed stator phase inductance	$(3.75 \pm 10\,\%)\,\mu H$
χ_{pm}	Radial bearing constant	$71.6 \cdot 10^{-3}$ Vs/m
U_{DC}	DC-link voltage	12 V
f_{sw}	Switching frequency	1 MHz
f_{bw}	Current controller bandwidth	12 kHz

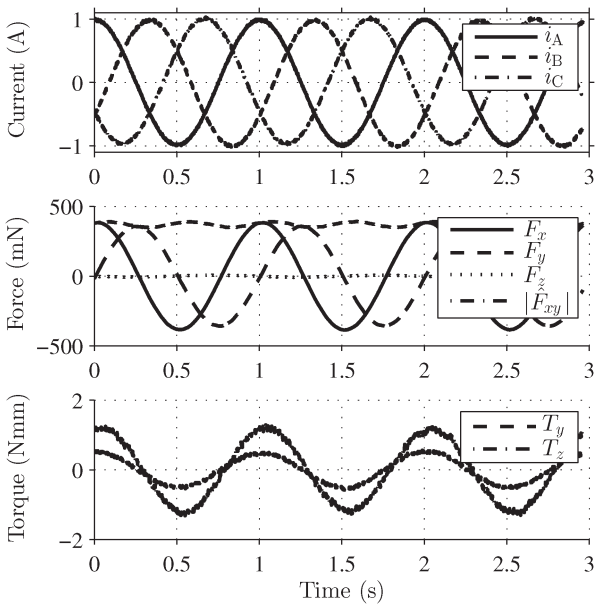

Fig. 10. Multidimensional dynamometer measurement of bearing force and torque generated by a skewed $p_w = 2$ test winding with an ironless stator $R_6 \to \infty$. Measurement setup parameters: $R_1 = 7.1$ mm, $R_3 = 8$ mm, $R_4 = 10$ mm, $L = 27.5$ mm, $N = 12$, and $B_{rem} = 1.1$ T.

A. Measurement of Bearing Force

In order to verify the presented bearing force calculations, a set of 3-D force and torque measurements have been performed. The permanent magnet used for this measurement is mounted on a rotational stage. The rotor is then inserted without mechanical contact into the stator. The stator is mounted on a piezoelectric multicomponent load cell (Kistler 9256C1) to measure the winding reaction force and torque components resulting from the injected winding currents. A Spitzenberger&Spies DM3000 power supply is used to generate the three-phase symmetric sinusoidal voltages applied to the star-connected winding at a frequency of $\omega = 2\pi \cdot 1$ Hz.

Measurement results are shown in Fig. 10 for an ironless stator $R_6 \to \infty$ configuration and a fixed angular position of $\gamma = 0$ and $\varepsilon = \omega t$. This allows measuring the Lorentz force solely. From (8), a bearing force amplitude $|\hat{F}_{xy}| = 350$ mN is expected, which corresponds well with the measured range of 345–375 mN. Furthermore, it can be seen that $|\hat{F}_{xy}|$ exhibits an oscillation of $\pm 4\%$ of its mean value. It is assumed that this effect is caused by small asymmetries of the phases caused by the two-layer winding structure [22]. It is expected that no torque $\boldsymbol{T}$ is generated. Indeed, a very small torque of less than 1.5 Nmm in amplitude was measured.

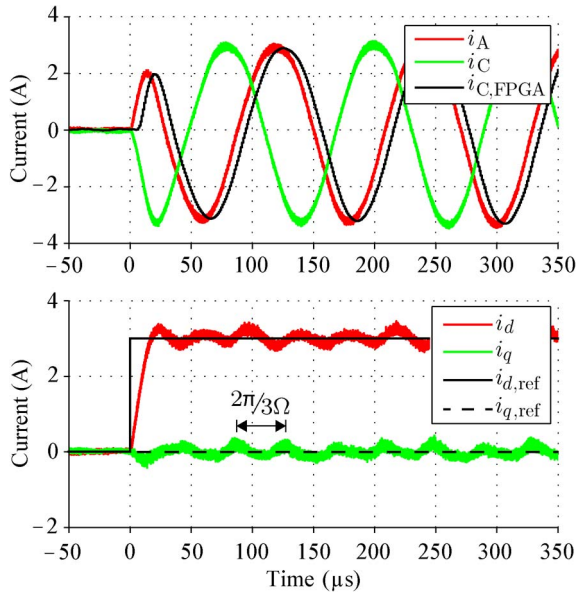

Fig. 11. Measured radial-bearing current step response due to a reference step in the d-direction for an angular frequency $\Omega = 2\pi \cdot 8.33$ kHz. The upper plot shows the phase currents i_A, i_C and the FPGA signal of the system-measured phase current $i_{A,FPGA}$. The lower plot shows the step response transformed into dq coordinates and references $i_{d,ref}$ and $i_{q,ref}$. The observed current ripple with a fundamental frequency of three times the rotational frequency is due to phase asymmetries of the bearing winding (cf. Table II).

The force measurement including an iron stator core $R_6 = R_4$ is marked with a cross in Fig. 7. The measured bearing force amplitude $|\hat{F}_{xy}|$ range of (593 $\pm$ 1.5%) mN corresponds well with the FEM-based value of 601 mN.

B. Power Electronics

Fig. 11 shows a bearing current step response for $\Omega = 2\pi \cdot 8.33$ kHz of the bearing inverter system, as shown in Fig. 8. For this measurement, the rotor was removed from the motor. This allows for an isolated performance evaluation of the PI controllers and decoupling scheme [cf. (20)] implemented in the inner current control loop of the cascaded control architecture. γ was artificially generated by a sine lookup table and could thus be used to obtain the step response in dq coordinates by means of postprocessing of the measured currents. The analysis shows that the current controller features the required bandwidth and accuracy at the target speed. Furthermore, a current ripple can be observed, which comprises a low- and a high-frequency content. Whereas the high-frequency current ripple has a fundamental frequency equal to $f_{sw} = 1$ MHz and is an inevitable consequence of the use of a switched-mode power converter, the low-frequency current ripple is caused by the phase asymmetry of the bearing winding (cf. Table II). This finding is consistent with the observed variation of the bearing force amplitude $|\hat{F}_{xy}|$, as shown in Fig. 10, where a similar skewed air-gap winding was used. The low-frequency ripple shows a fundamental frequency of three times the rotational frequency. For high rotor speeds ($\Omega \gtrsim 2\pi \cdot 4$ kHz), this frequency lies outside the controller bandwidth $f_{bw} = 12$ kHz and cannot thus be controlled. However, the occurring ripple currents will solely moderately increase the losses in the

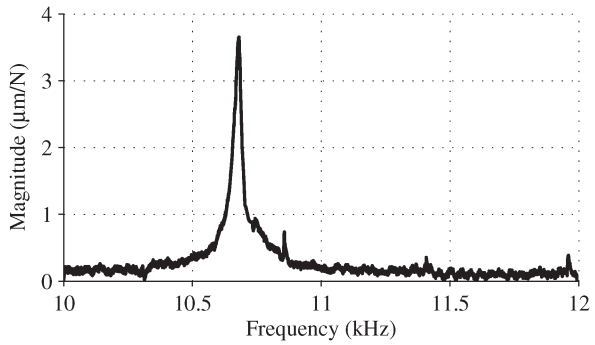

Fig. 12. Frequency measurement of the first rotor bending mode resonance at standstill.

winding but not affect the mechanical system. The latter is a consequence of the high frequency, which is far beyond the mechanical bandwidth [21].

C. Rotor Bending Resonance Measurement

A fundamental limitation of the maximum rotational speed is the frequency of the first rotor bending mode. Due to the stiff rotor construction, the high frequency of the resonance, and the high internal damping of the rotor, exciting the bending resonance by a reference position step input was not possible. Therefore, a sine wave excitation was used for the measurement. A rotating radial force is applied to the levitated rotor by the magnetic bearing. The resulting rotor tip displacement is measured by an external optical displacement sensor (Keyence LK-H022). A measurement of the transfer function from distorting force to rotor displacement can be obtained by sweeping the frequency of the distortion while measuring the rotor tip displacement [25]. Increased displacements at the resonance frequency follow from the bending of the rotor. A measurement of the transfer function around the first bending mode is shown in Fig. 12. The measured resonance frequency of 10.7 kHz is about 10% lower than the calculated frequency of 11.9 kHz. This difference might be caused by an aberration from the specified material properties or by manufacturing tolerances.

D. Closed-Loop System Measurements

Fig. 13 shows rotor displacements for different speeds measured by one of the PCB-based eddy-current sensors with a sampling frequency of 33 kHz. The sensor measures radial rotor displacements in an axial distance of 6.4 mm from the rotor tip. Given the high rotational speed, an external 1-D ultrahigh-speed optical displacement sensor (Keyence LK-H022) with a sampling frequency of 100 kHz is used to track the rotor tip displacement at 500 kr/min in Fig. 14. In contrast to the eddy-current sensor, the optical sensor is positioned to measure the radial rotor displacements at the rotor tip. An Ω-synchronous displacement of about ± 17 μm can be observed. Due to the frequency and the fact that larger displacements are measured at the rotor tips, it is assumed that the displacements are caused by the unbalance of the rotor. The rotor could not be balanced during manufacturing as it is intended for high speeds.

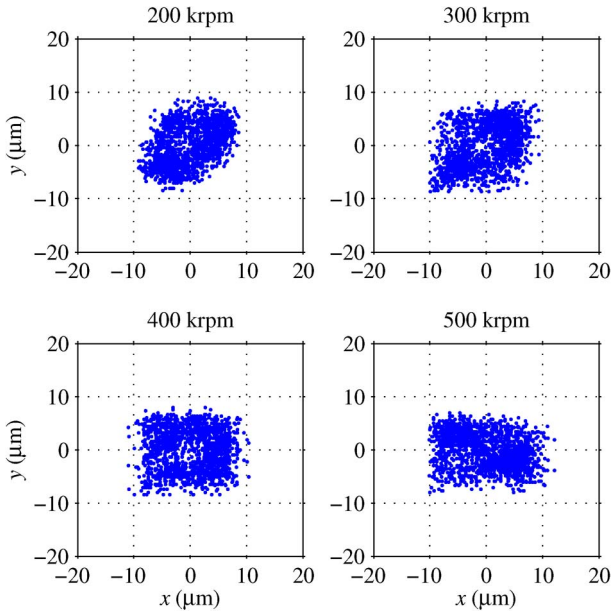

Fig. 13. Measured radial rotor displacements. The measurements are obtained by the PCB-based eddy-current sensor.

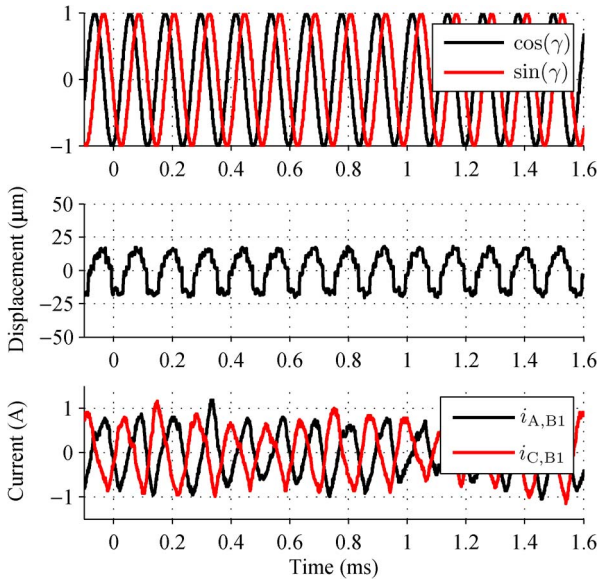

Fig. 14. Closed-loop system measurement of a spinning rotor at 500 kr/min. The upper plot shows the Hall-effect-based angular rotor position measurement. The center plot shows the radial rotor tip displacement in the x-axis direction measured by an external optical displacement sensor. The measured bearing phase currents $i_{A,B1}$, $i_{C,B1}$ are shown in the lower plot.

In Fig. 15, the result of an acceleration and reference speed tracking test is shown.

E. Power Loss Measurements

Due to the high speed and the low torque of the presented machine, a loss measurement based on a rotary torque transducer is not applicable [1]. Therefore, the no-load losses are measured by means of a deceleration test. The rotor is accelerated to 505 kr/min, after which the motor inverter is switched off, letting the losses decelerate the rotor [1]. The recorded speed versus time is shown in Fig. 16. The breaking losses, consisting

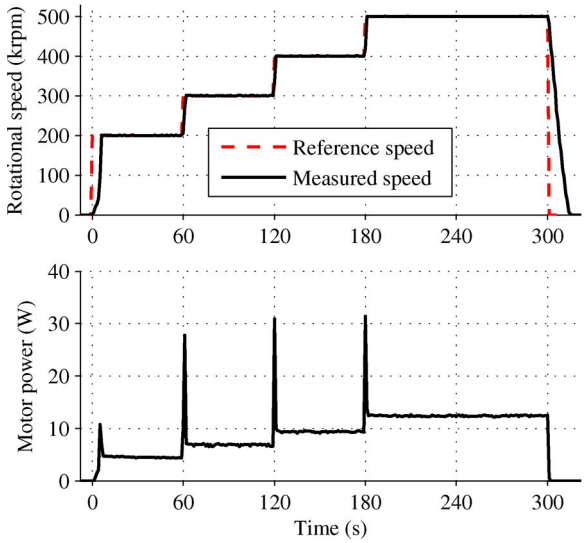

Fig. 15. Reference speed tracking and motor power in vacuum.

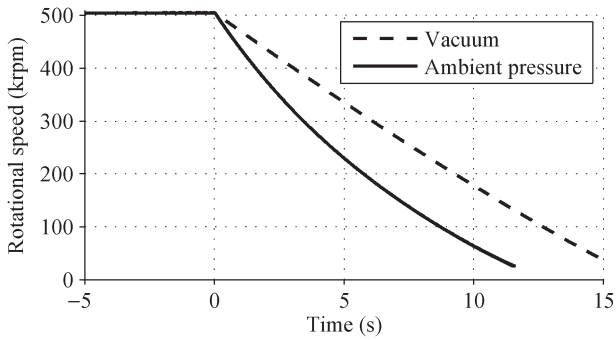

Fig. 16. Deceleration test measurement at 505 kr/min in vacuum and ambient air-pressure conditions.

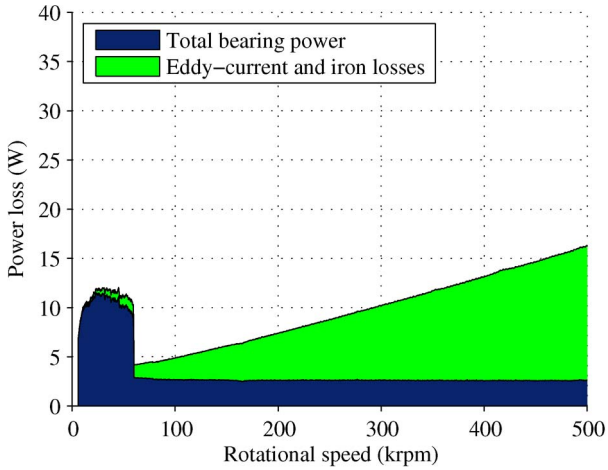

Fig. 17. Measured no-load power loss in vacuum.

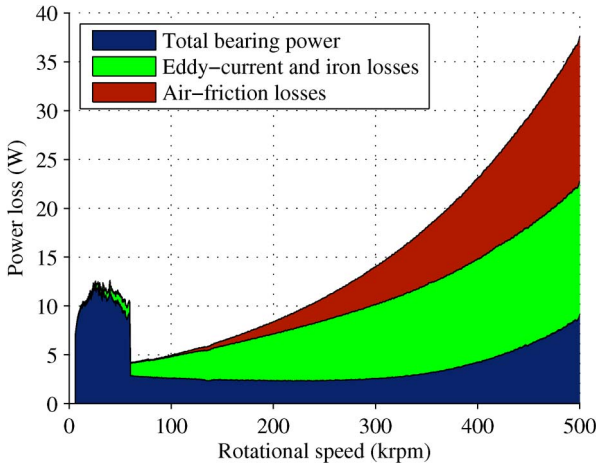

Fig. 18. Measured no-load power loss in ambient air-pressure conditions.

of eddy-current, iron, and air-friction losses, are calculated using the known moment of inertia of the rotor. The measurement is performed in vacuum and repeated in ambient air-pressure conditions. The ambient air test setup is shown in Fig. 4 and the vacuum test setup in Fig. 5. With the measured losses of both experiments, the air-friction losses can be separated from the rest. Using the presented measurement method, the eddy-current losses and iron losses cannot be separated from each other. The total magnetic bearing power is measured, during the deceleration, by measuring the bearing inverter dc-link input power. Thus, the measured total bearing power consists of switching losses and conduction losses in the bearing inverter and winding system.

Figs. 17 and 18 show the measured power loss in vacuum and in ambient air-pressure conditions, respectively. Both plots feature a distinctive bearing power drop at 60 kr/min. This loss reduction is achieved by enabling a rotor position notch filter, as described in [26], for rotational frequencies above the cutoff frequency of the mechanical bearing system, i.e., for speeds above 60 kr/min. The purpose of the notch filter is to reduce the power loss in the bearing windings. In vacuum, the bearing power features practically no speed dependence over 60 kr/min. In ambient air-pressure conditions, the bearing power increases for speeds above 300 kr/min because the parasitic aerodynamic forces acting on the rotor have to be compensated by the magnetic bearing.

The measured sum of the eddy-current and iron losses is 13.7 W at 500 kr/min. Based on field simulations, it can be assumed that approximately 80% of these losses are due to eddy currents in the nonlaminated stator aluminum. The eddy currents are caused by the stray field of the permanent magnets in the aluminum parts of the stator that are used as the thermal connection of the bearing windings with the rest of the stator. Proximity losses in the windings of 0.9 W and iron losses of 1.8 W are expected from calculations. The proximity losses are calculated using the Ferreira method presented in [27].

VI. Conclusion

The slotless self-bearing motor prototype presented in this paper overcomes several limitations of previously presented high-speed magnetic bearings. The ironless construction of the rotor and the slotless design of the stator enable ultrahigh-speed rotation and very high bearing actuator bandwidths. A mechanical and electrical bearing model is presented and verified by multidimensional force measurements. It is shown that the bearing actuators feature linear characteristics. In order to control the bearing currents, an inverter system is designed

using a switching frequency of 1 MHz, and its controller performance is shown. Closed-loop system measurements up to speeds of 505 kr/min verify the functionality of the overall system. To the authors' knowledge, this is the highest speed achieved by magnetically levitated electrical drive systems so far.

ACKNOWLEDGMENT

The authors would like to thank C. Zwyssig and M. Bartholet from Celeroton AG for their support; M. Vohrer from ATE GmbH for manufacturing the windings; and P. Schütz and T. Lüthi from Swiss Federal Laboratories for Materials, Science, and Technology (EMPA) for helping in analyzing and improving the rotor construction.

REFERENCES

[1] J. Luomi, C. Zwyssig, A. Looser, and J. W. Kolar, "Efficiency optimization of a 100-W 500 000-r/min permanent-magnet machine including air-friction losses," *IEEE Trans. Ind. Appl.*, vol. 45, no. 4, pp. 1368–1377, Jul./Aug. 2009.

[2] D. Krähenbühl, C. Zwyssig, and J. W. Kolar, "Half-controlled boost rectifier for low-power high-speed permanent-magnet generators," *IEEE Trans. Ind. Electron.*, vol. 58, no. 11, pp. 5066–5075, Nov. 2011.

[3] S. Silber, J. Sloupensky, P. Dirnberger, M. Moravec, M. Reisinger, and W. Amrhein, "High speed drive for textile rotor spinning applications," *IEEE Trans. Ind. Electron.*, vol. 61, no. 6, pp. 2990–2997, Jun. 2014.

[4] M. Kimman, H. Langen, and R. M. Schmidt, "A miniature milling spindle with active magnetic bearings," *Mechatronics*, vol. 20, no. 2, pp. 224–235, Mar. 2010.

[5] F. Betschon, "Design principles of integrated magnetic bearings," Ph.D. dissertation, ETH Zurich, Zurich, Switzerland, 2000.

[6] G. Schweitzer and E. H. Maslen, *Magnetic Bearings*. New York, NY, USA: Springer-Verlag, 2009.

[7] T. Baumgartner, A. Looser, C. Zwyssig, and J. W. Kolar, "Novel high-speed, Lorentz-type, slotless self-bearing motor," in *Proc. IEEE ECCE*, Sep. 2010, pp. 3971–3977.

[8] H. Mitterhofer and W. Amrhein, "Design aspects and test results of a high speed bearingless drive," in *Proc. 9th IEEE Int. Conf. PEDS*, Dec. 2011, pp. 705–710.

[9] Z. Ren and L. Stephens, "Force characteristics and gain determination for a slotless self-bearing motor," *IEEE Trans. Magn.*, vol. 42, no. 7, pp. 1849–1860, Jul. 2006.

[10] T. Grochmal and A. Lynch, "Control of a self-bearing servomotor," *IEEE Control Syst.*, vol. 29, no. 5, pp. 74–92, Oct. 2009.

[11] T. Reichert, T. Nussbaumer, and J. W. Kolar, "Bearingless 300-W PMSM for bioreactor mixing," *IEEE Trans. Ind. Electron.*, vol. 59, no. 3, pp. 1376–1388, Mar. 2012.

[12] B. Warberger, R. Kaelin, T. Nussbaumer, and J. W. Kolar, "50-Nm/2500-W bearingless motor for high-purity pharmaceutical mixing," *IEEE Trans. Ind. Electron.*, vol. 59, no. 5, pp. 2236–2247, May 2012.

[13] J. Asama, Y. Hamasaki, T. Oiwa, and A. Chiba, "Proposal and analysis of a novel single-drive bearingless motor," *IEEE Trans. Ind. Electron.*, vol. 60, no. 1, pp. 129–138, Jan. 2013.

[14] Q. D. Nguyen and S. Ueno, "Analysis and control of nonsalient permanent magnet axial gap self-bearing motor," *IEEE Trans. Ind. Electron.*, vol. 58, no. 7, pp. 2644–2652, Jul. 2011.

[15] J. W. Beams, J. L. Young, and J. W. Moore, "The production of high centrifugal fields," *J. Appl. Phys.*, vol. 17, no. 11, pp. 886–890, Nov. 1946.

[16] B. E. Kane, "Levitated spinning graphene flakes in an electric quadrupole ion trap," *Phys. Rev. B*, vol. 82, no. 11, pp. 115441–1–11544–13, Sep. 2010.

[17] T. Reichert, T. Nussbaumer, and J. W. Kolar, "Complete analytical solution of electromagnetic field problem of high-speed spinning ball," *J. Appl. Phys.*, vol. 112, no. 10, pp. 104901–1–104901–9, Nov. 2012.

[18] A. Looser and J. W. Kolar, "A hybrid bearing concept for high-speed applications employing aerodynamic gas-bearings and a self-sensing active magnetic damper," in *Proc. 37th Annu. IEEE IECON*, 2011, pp. 1686–1691.

[19] T. Baumgartner, R. Burkart, and J. W. Kolar, "Analysis and design of an ultra-high-speed slotless self-bearing permanent-magnet motor," in *Proc. 38th Annu. IEEE IECON*, Oct. 2012, pp. 4477–4483.

[20] A. Looser, T. Baumgartner, C. Zwyssig, and J. W. Kolar, "Analysis and measurement of 3D torque and forces for permanent magnet motors with slotless windings," in *Proc. IEEE ECCE*, Sep. 2010, pp. 3792–3797.

[21] T. Baumgartner and J. W. Kolar, "Multivariable state feedback control of a 500 000 rpm self-bearing motor," in *Proc. IEEE IEMDC*, May 2013, pp. 347–353.

[22] A. Looser, T. Baumgartner, J. W. Kolar, and C. Zwyssig, "Analysis and measurement of three-dimensional torque and forces for slotless permanent-magnet motors," *IEEE Trans. Ind. Appl.*, vol. 48, no. 4, pp. 1258–1266, Jul./Aug. 2012.

[23] K. Sridhar, "Electromagnetic models for slotless PM synchronous motor drives," in *Proc. IEEE APEC Expo.*, Mar. 1995, pp. 367–377.

[24] D. G. Holmes, B. P. McGrath, and S. G. Parker, "Current regulation strategies for vector-controlled induction motor drives," *IEEE Trans. Ind. Electron.*, vol. 59, no. 10, pp. 3680–3689, Oct. 2012.

[25] R. Isermann and M. Munchhof, *Identification of Dynamic Systems*. New York, NY, USA: Springer-Verlag, 2001.

[26] R. Herzog, P. Buhler, C. Gahler, and R. Larsonneur, "Unbalance compensation using generalized notch filters in the multivariable feedback of magnetic bearings," *IEEE Trans. Control Syst. Technol.*, vol. 4, no. 5, pp. 580–586, Sep. 1996.

[27] J. A. Ferreira, *Electromagnetic Modeling of Power Electronic Converters*. Norwell, MA, USA: Kluwer, 1989.

Thomas Baumgartner (S'10) received the M.Sc. degree in electrical engineering in 2009 from the Swiss Federal Institute of Technology (ETH) Zurich, Zurich, Switzerland, where he is currently working toward the Ph.D. degree at the Power Electronic Systems Laboratory, working on magnetic bearings for ultrahigh-speed drive systems.

He was with the Automatic Control Laboratory, ETH Zurich, where he was involved in the field of trajectory prediction algorithms for low-cost collision avoidance systems.

Ralph M. Burkart (S'12) received the M.Sc. degree (with distinction) in electrical engineering in 2011 from the Swiss Federal Institute of Technology (ETH) Zurich, Zurich, Switzerland, where he is currently working toward the Ph.D. degree at the Power Electronic Systems Laboratory, working on high-dynamic inverter systems for high-speed active magnetic bearings and comparative studies on inverter topologies for photovoltaic applications.

During his studies, he focused on power electronics, electrical machines, and control.

Johann W. Kolar (M'89–SM'04–F'10) received the M.Sc. and Ph.D. degrees (*summa cum laude/promotio sub auspiciis praesidentis rei publicae*) from the Vienna University of Technology, Vienna, Austria, in 1997 and 1998, respectively.

Since February 1, 2001, he has been a Professor and the Head of the Power Electronic Systems Laboratory, Swiss Federal Institute of Technology (ETH) Zurich, Zurich, Switzerland. He has proposed numerous novel pulsewidth modulation converter topologies, and modulation and control concepts, e.g., the Vienna rectifier, the Swiss rectifier, and the three-phase ac–ac sparse matrix converter. He has published over 550 scientific papers in international journals and conference proceedings, and has filed more than 110 patents.